ACS OMEGA

http://pubs.acs.org/journal/acsodf

Article

Synthesis and Characterization of MC/TiO_2 NPs Nanocomposite for Removal of Pb^{2+} and Reuse of Spent Adsorbent for Blood Fingerprint Detection

Yvonne Boitumelo Nthwane, Bienvenu Gael Fouda-Mbanga, Melusi Thwala, and Kriveshini Pillay*

Cite This: *ACS Omega* 2023, 8, 26725−26738

Read Online

ACCESS | Metrics & More | Article Recommendations

ABSTRACT: The removal of toxic heavy metals from wastewater through the use of novel adsorbents is expensive. The challenge arises after the heavy metal is removed by the adsorbent, and the fate of the adsorbent is not taken care of. This may create secondary pollution. The study aimed to prepare mesoporous carbon (MC) from macadamia nutshells coated with titanium dioxide nanoparticles (TiO_2 NPs) using a hydrothermal method to remove Pb^{2+} and to test the effectiveness of reusing the lead-loaded spent adsorbent (Pb^{2+}-MC/TiO_2 NP nanocomposite) in blood fingerprint detection. The samples were characterized using SEM, which confirmed spherical and flower-like structures of the nanomaterials, whereas TEM confirmed a particle size of 5 nm. The presence of functional groups such as C and Ti and a crystalline size of 4 nm were confirmed by FTIR and XRD, respectively. The surface area of 1283.822 m^2/g for the MC/TiO_2 NP nanocomposite was examined by BET. The removal of Pb^{2+} at pH 4 and the dosage of 1.6 g/L with the highest percentage removal of 98% were analyzed by ICP-OES. The Langmuir isotherm model best fit the experimental data, and the maximum adsorption capacity of the MC/TiO_2 NP nanocomposite was 168.919 mg/g. The adsorption followed the pseudo-second-order kinetic model. The $\Delta H°$ (−54.783) represented the exothermic nature, and $\Delta G°$ (−0.133 to −4.743) indicated that the adsorption process is spontaneous. In the blood fingerprint detection, the fingerprint details were more visible after applying the Pb^{2+}-MC/TiO_2 NP nanocomposite than before the application. The reuse application experiments showed that the Pb^{2+}-MC/TiO_2 NP nanocomposite might be a useful alternative material for blood fingerprint enhancement when applied on nonporous surfaces, eliminating secondary pollution.

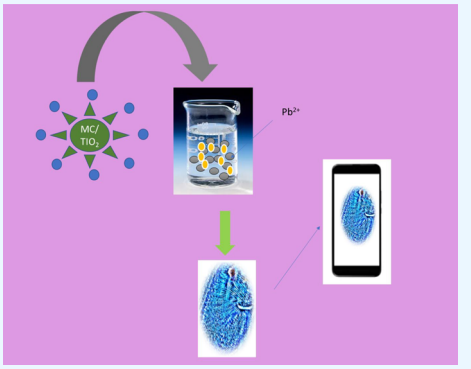

1. INTRODUCTION

The presence of heavy metals (HMs) in water environments may result in harmful effects in both ecological and human life. Some HMs, such as chromium (Cr), cadmium (Cd), lead (Pb), cobalt (Co), and nickel (Ni), may lead to adverse side effects when entering water systems.[1,2] Regarding the harmful impacts, Pb^{2+} is among the highly toxic types of HMs absorbed by the human body and may lead to cancer, nervous system damage, organ failure, and even mortality.[3,4] The anthropogenic sources of Pb^{2+} in the environment include mining and industrial processes such as petroleum refining, pulp and paper operations, plastic and fertilizer manufacturing, electroplating, and metallurgical processes.[5,6] The World Health Organization (WHO) has estimated the maximum permissible limit of Pb^{2+} in drinking water to be 0.05 mg/L, and the allowable limit (mg/L) given by Environmental Protection Agency for Pb^{2+} in wastewater is determined to be 0.05 mg/L.[7,8] The target water quality range for sufficient ecological health protection is 60−180 μg/L between soft and very hard water.[9] In industrial wastewater, lead-ion concentrations approach 200−500 mg/L.[8] However, developing methods at a cheaper cost is needed to reduce lead-ion concentrations to a level of 0.05−0.10 mg/L before they can be discharged into the water or sewage systems.[10]

Several techniques, such as reverse osmosis,[11] membrane filtration,[12] precipitation,[13] ion exchange,[14] phytoremediation,[15] and adsorption[16] have been employed to treat HMs in water.[17] However, these techniques require special operational skills; they are expensive and time-consuming.[18] For these reasons, much work has focused on adsorption. Adsorption is an attractive technique due to its low cost, easy operation, simple design, and effectiveness in treating HMs in water.[19] Most researchers are developing different adsorbents for water treatment.[20−24] However, the adsorbent requires regeneration.[25] Commercial carbons are generally

Received: September 5, 2022
Accepted: March 14, 2023
Published: July 17, 2023

Scheme 1. Preparation of Carbon-Derived Macadamia Nutshells

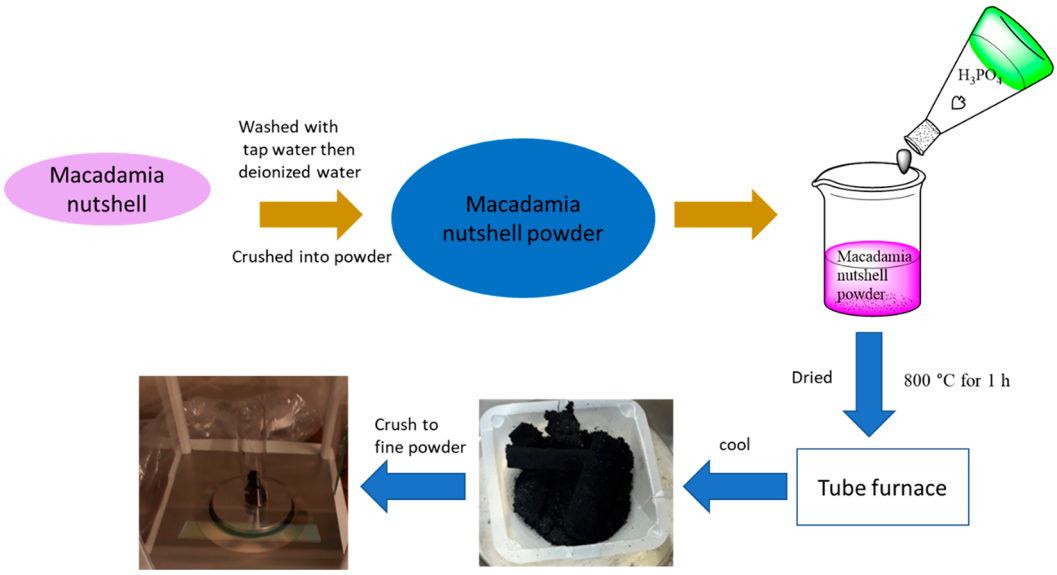

expensive, and agricultural, natural, and industrial waste makes adsorption inexpensive. Agricultural waste has become attractive as a remediation adsorbent for HMs due to its relative accessibility compared to solid industrial waste materials. Macadamia nutshells as agricultural waste have been used to remove HMs,[26−28] and South Africa is the third-largest producer of this waste material.[29] Their functional groups include aldehydes, ethers, ketones, alcohols, and esters.[30]

Agricultural wastes are mainly used as carbons for water treatment when burned at higher temperatures. Carbon nanomaterials, including activated carbon (e.g., mesoporous carbon: MC), carbon dots, graphene, carbon nanotubes, fullerenes, and graphite, can be coated with metal oxides such as titanium dioxide (TiO_2), zinc oxide (ZnO), and cerium oxide (CeO_2) for HMs' remediation. The carbon nanomaterials[31] coated with metal oxide[32] are favored to increase the surface area, porosity, and binding sites. Mesoporous carbon-coated TiO_2 NPs have been reported in the literature but mainly focus on photocatalysis[33] and energy applications.[34] Metal oxides such as ZnO, Al_2O_3, and TiO_2 also have the advantages of a porous structure, low cost, physicochemical stability, ease of availability, and high surface area.[35] Among them, TiO_2 NPs are the cheapest, most nontoxic, and most stable materials.[36,37] Hence, TiO_2 NPs were identified as the best metal oxide to use in this study.

However, while adsorption has its advantages, it also has the disadvantage of generating an undesirable spent adsorbent which causes secondary environmental pollution. Hence, studying the reuse applications of the spent adsorbent has become imperative. In recent years, spent adsorbents have been reused for catalytic,[38,39] photocatalytic,[40,41] and forensic applications.[42−44] Fingerprint detection has been chosen because it will solve the secondary pollution issue and simultaneously solve problems with crime investigations.

During criminal activity (it can be physical violence, sexual violence, or murder), the perpetrators may not be convicted due to insufficient evidence linking them to the crime scene. Crime scene samples can be collected to gather evidence, including saliva, blood, semen, and fingerprints. A blood fingerprint (BFP) is a crucial piece of evidence that has been used for over 150 years to link suspects to crime scenes potentially. They can be obtained on a porous surface such as clothing items, toilet paper, raw wood, or cardboard and nonporous surfaces such as tiles, glass, knives, windows, and other things. Several publications have focused on developing materials for latent fingerprints,[45] and carbon-coated metal oxides are one of the materials used as labeling agents to visualize the fingerprints.[46,47] Other materials enhancing friction ridges include carbon nanomaterials[48] and metal oxides.[49] The quality of fingerprint photographs has been improved by forensic researchers using various physical and chemical techniques, such as powder dusting methods, fluorescent probes, cyanoacrylate fuming, and spray methods.[50−52] The powder dusting method has been thoroughly investigated for latent fingerprint enhancement using various powders such as luminous powders, magnetic powders, and metallic particles.[53−55]

Therefore, this study aimed to prepare an MC/TiO_2 NP nanocomposite material for Pb(II) remediation and investigate the reuse of the lead-loaded spent adsorbent (Pb^{2+}-MC/TiO_2 NP nanocomposite) for blood fingerprint identification/detection. Even though numerous papers have been published on carbon nanomaterials such as mesoporous carbon and metal oxides such as TiO_2 NPs, those studies did not focus on the end-of-life of pollutants adsorbed from wastewater. Investigations have been conducted using metal-loaded adsorbents removed from wastewater for latent fingerprint detection.[42−44] However, these studies did not focus on the detection of blood fingerprints. The current study intends to use an effective nanomaterial for water remediation and to eliminate secondary pollution by reusing the Pb^{2+}-MC/TiO_2 NP nanocomposite to help law enforcement officials solve crimes by quickly detecting latent fingerprints in the blood.

2. MATERIALS AND METHODS

Macadamia nutshells were collected from a farm (Mpumalanga, South Africa). Titanium(IV) isopropoxide (pure, ≥97%), nitric acid (HNO_3, ≥65%), cupric(II) nitrate trihydrate ($Cu(NO_3)_2{\cdot}3H_2O$, >99−104%), cadmium(II) nitrate tetrahydrate ($Cd(NO_3)_2{\cdot}4H_2O$, >98%; $Ni(NO_3)_2{\cdot}6H_2O$, >98%), sodium hydroxide (NaOH, >99.9%), lead(II) nitrate

https://doi.org/10.1021/acsomega.2c05765
ACS Omega 2023, 8, 26725−26738

Scheme 2. Synthesis of Mesoporous Carbon-Coated TiO_2NPs Nanocomposite

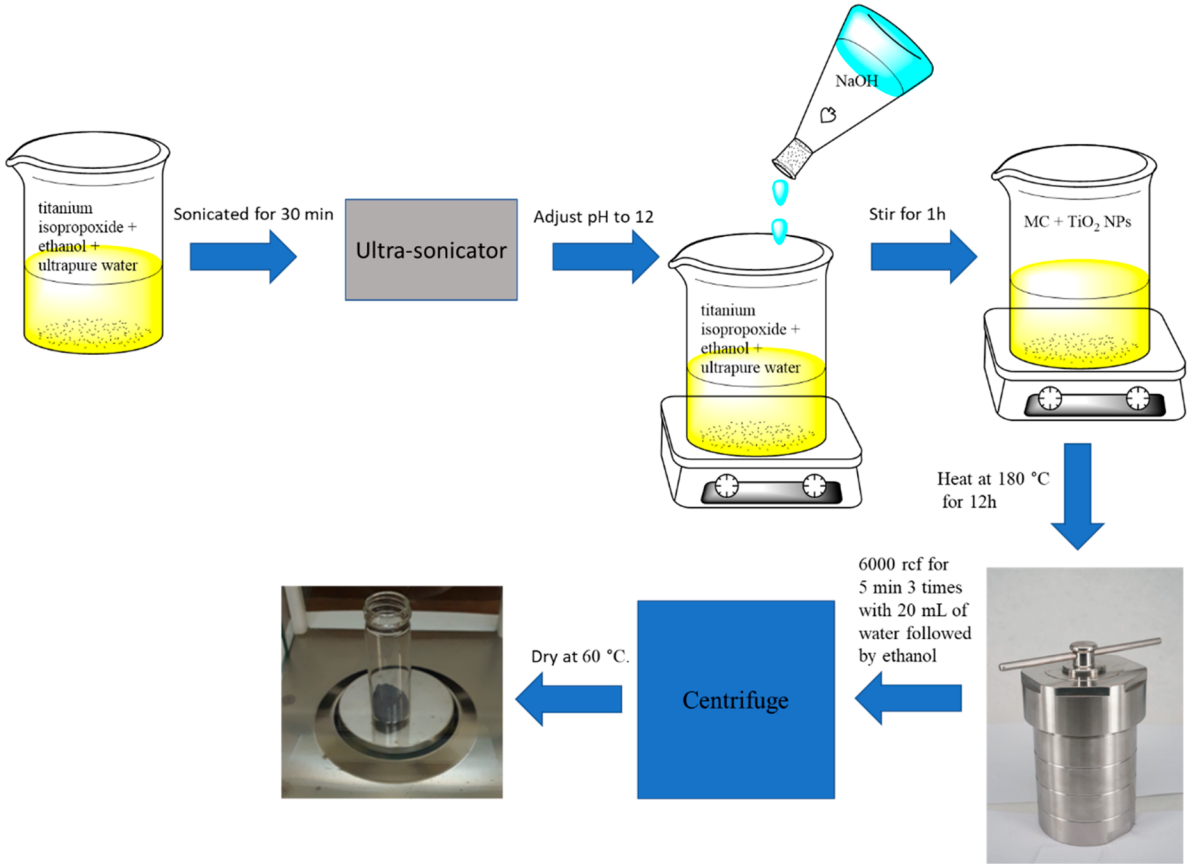

($Pb(NO_3)_2$, >99.99%), and phosphoric acid (H_3PO_4, >99.99%) were purchased from Sigma-Aldrich (Pretoria, South Africa) and were used without any further purification. Ethanol (pure, ≥99.8%), potassium bromide (pure, ≥99.0%), and hydrochloric acid (>37%) were purchased from Merck (Johannesburg, South Africa). Hemoglobin powder was purchased from Shanghai Richem International, and paintbrushes were purchased from local markets.

2.1. Preparation of Mesoporous Carbon-Derived Macadamia Nutshell. MC was synthesized using a slight modification to a previously published procedure.[56] In a typical procedure, about 200 g of macadamia nutshells were collected, washed with tap water followed by type 1 ultrapure deionized water to remove all the dirt, and dried in an oven at 60 °C overnight. The macadamia nutshells were ground into a fine powder using a mortar and pestle and sieved. H_3PO_4 (20 mL) was added to 20.011 g of macadamia nutshell and then dried at 60 °C. The pretreated macadamia nutshell was placed in a quartz tube and then in the tube furnace and heated at 800 °C for 1 h. The obtained mesoporous carbon was crushed into a fine powder with a mortar and pestle. Scheme 1 illustrates the preparation of mesoporous carbon-derived macadamia nutshells.

2.2. Preparation of Mesoporous Carbon-Coated TiO_2NPs. The coating of MC to TiO_2 NPs was prepared following a previously described procedure.[42] In a glass beaker, 5 mL of titanium isopropoxide was added to 20 mL of ethanol, and 20 mL of ultrapure water was placed in an ultrasonicator for 30 min. Sodium hydroxide was added dropwise under vigorous stirring to adjust the pH to 12. The mesoporous carbon was added into a suspension of TiO_2 NPs and then stirred for 1 h. The solution was transferred into a capacitive Teflon-lined stainless steel autoclave reactor for 12 h at 180 °C. The sample was centrifuged at 6000 rcf for 5 min three times with 20 mL of water followed by ethanol and then dried at 60 °C. Scheme 2 illustrates the synthesis of a mesoporous carbon-coated TiO_2 NP nanocomposite.

2.3. Characterization Techniques. The functional groups of the MC/TiO_2 NP nanocomposite were analyzed by Fourier transform infrared spectroscopy (FTIR) in the range of 4000−400 cm^{-1} using the KBr pellet method (PerkinElmer, USA). To examine the surface morphological structure of MC, TiO_2 NPs, and the MC/TiO_2 NP nanocomposite, samples were prepared by coating them with a carbon coating, then analyzed by scanning electron microscopy (SEM-Tescanvega 3xmu), and the MC/TiO_2 NP nanocomposite was dispersed in ethanol then sonicated for 10 min. The size was analyzed by transmission electron microscopy (TEM, JEOL JEM-2100F, Japan) with an electron accelerating voltage of 90 kV. The MC/TiO_2 NP nanocomposites were dispersed in deionized water. Then, pH was measured and sonicated, and zeta potential was analyzed using a Malvern Zetasizer NanoZS 90. The Pb^{2+} concentration was conducted using inductively coupled plasma−optical emission spectrometry (ICP-OES, Shimadzu, Japan). A Remi Orbital Shaker was used for shaking the solution. X-ray powder diffraction (XRD) using Cu$K\alpha$ radiation was used to examine the crystallinity of the samples (Ultima IV, Rigagu, Japan). The samples were dried and heated in an oven (Binder, FD 53, USA). Brunauer−Emmett−Teller (BET) was used to examine the surface area, and pore volume material was prepared by nitrogen adsorption−desorption measurements with degassing

https://doi.org/10.1021/acsomega.2c05765
ACS Omega 2023, 8, 26725−26738

at 100 °C for 6 h using Micrometrics, ASAP 2020. Thermogravimetric analyses (TGA) were used to determine the thermal stability of the sample using TGA Q500 (TA Instruments, USA). Blood fingerprint images were captured using a smartphone.

2.4. Batch Adsorption Experiment. In a 1000 mL volumetric flask, 50 ppm of Pb^{2+} was prepared by weighing out 0.08 g of lead nitrate, which was added to 100 mL of deionized water. Batch adsorption studies were carried out using 2 g/L of the MC/TiO_2 NP nanocomposite in a 50 mL aqueous solution of 50 ppm Pb^{2+} at pH 4. The pH was adjusted using 0.1 M HCl and 0.1 M NaOH to pH 4. Then, 100 mL plastic bottles containing 50 mL Pb^{2+} solution were agitated in a shaker for 2 h at 25 °C and then filtered using a 0.45 um PES syringe filter. The adsorption capacity of the Pb^{2+} ion from an aqueous solution by the MC/TiO_2 NP nanocomposite was calculated using the following equation, eq 1:

$$q_e = \frac{[(C_o - C_e) \times V]}{m} \quad (1)$$

where q_e (mg/g) is the adsorption capacity of Pb^{2+}, C_o (mg/L) represents the initial concentration, C_e (mg/L) is the equilibrium concentration of Pb^{2+}, V (L) is the volume of the aqueous solution, and m (g) is the adsorbent dosage. The removal rate of Pb^{2+} was calculated using eq 2.

$$\%\ \text{adsorption} = \frac{C_o - C_e}{C_o} \times 100 \quad (2)$$

The adsorbent was further used to determine the adsorption kinetics and isotherms. Adsorption isotherms were investigated at 25, 35, 45, and 55 °C by varying the concentrations at 50−300 ppm and further calculating the thermodynamic parameters such as enthalpy ($\Delta H°$), entropy ($\Delta S°$), and Gibbs free energy ($\Delta G°$). Adsorption isotherm experimental data were used to estimate the adsorption mechanism and equilibrium data. The adsorption kinetics were also studied from 30 to 180 min by varying the concentration from 50 to 300 pm at pH 4 using 1.6 g/L of the adsorbent. The adsorption rate of Pb^{2+} ion removal at time t was calculated using eq 3.

$$q_t = \frac{[(C_o - C_t) \times V]}{m} \quad (3)$$

where q_t (mg/g) and C_t (mg/L) are the adsorption capacity and concentration of Pb^{2+} ions at time t, respectively.

$$\sigma = \sqrt{\frac{\sum (X_i - \mu)^2}{N}}$$

σ is the standard deviation, N is the number of all values in the data set, X_i is each value in the data set, and μ denotes the mean of all values in the data set. All tests were done in triplicate to validate the experimental value.

2.5. Forensic Applications. *2.5.1. Preparation of Hemoglobin.* Approximately 5 g of hemoglobin was added to 250 mL of deionized water and then sonicated for 15 min, followed by heating at 50 °C for 45 min. The prepared hemoglobin was allowed to cool and kept in the refrigerator for further use.

2.5.2. Deposition of Blood Fingerprints. For blood fingerprint enhancement, three different surfaces were used, namely, glass, mirror, and aluminum sheets. Two volunteers were asked to wash their hands with soap and water thoroughly with ethanol. Commercial hemoglobin was taken with the micropipette, then dropped on the surface, and then smeared on the surface (glass, mirror, aluminum sheet) using a glass slide. The volunteers pressed their fingertips on the surface and allowed them to dry. The dust powder method was used for fingerprint detection. In the dust powdering method, the Pb^{2+}-MC/TiO_2 NP nanocomposite was dusted on different surfaces containing commercial hemoglobin and fingerprints using a paintbrush. The fingerprint images were captured on various surfaces using a smartphone camera.

3. RESULTS AND DISCUSSION

3.1. FTIR. The FTIR spectrum was used to characterize the functional groups of the MC/TiO_2 NP nanocomposite and MC, as shown in Figure 1c, i and ii. The broad characteristic

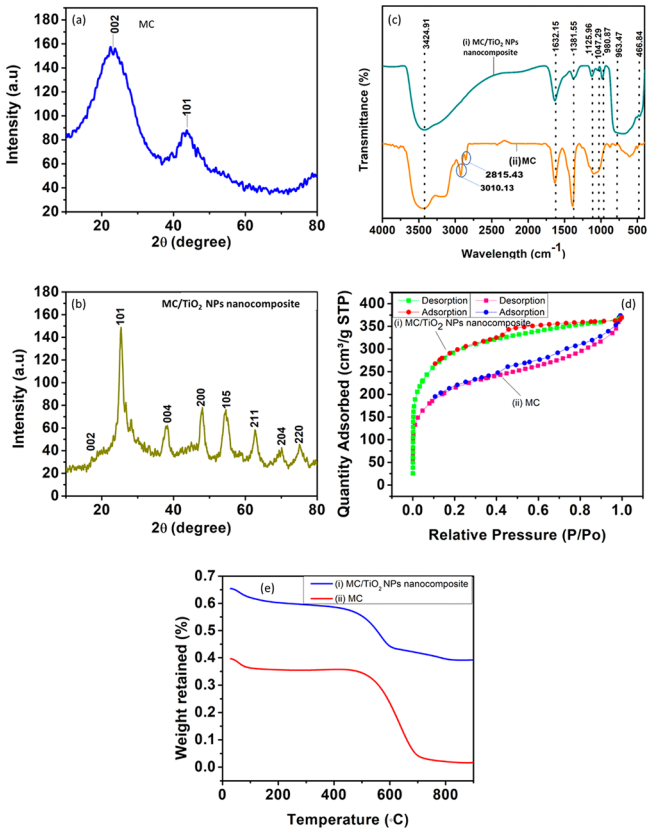

Figure 1. XRD patterns of (a) MC, (b) the MC/TiO_2 NP nanocomposite, FTIR spectra of (c, i) MC and (ii) MC/TiO_2 nanocomposite, (d) N_2 adsorption−desorption isotherm curve of (i) MC and (ii) MC/TiO_2 NP nanocomposite, (e) TGA curve of (i) MC/TiO_2 NP nanocomposite (ii) MC.

band at 3424.91 cm^{-1} is attributed to the hydroxyl and carbonyl groups. The bands at 1632.15, 1381.55, 1047.29, and 1125.96 cm^{-1} correspond to C−O, C−H, COO, and C═O that were introduced during the synthesis of mesoporous carbon, Figure 1c, ii. The additional bands detected at 2850 and 3010 are attributed to C−H stretching vibration and C−H aromatic structure.[57,58] The strong band formed at 1632.15 cm^{-1} may be attributed to C═O stretching in the carboxylate and ketone, as a result of acidic treatment. The rise in peak intensity at 1047.29 and 1125.96 cm^{-1} corresponds to the activation of different O-containing groups on the surface of

https://doi.org/10.1021/acsomega.2c05765
ACS Omega 2023, 8, 26725−26738

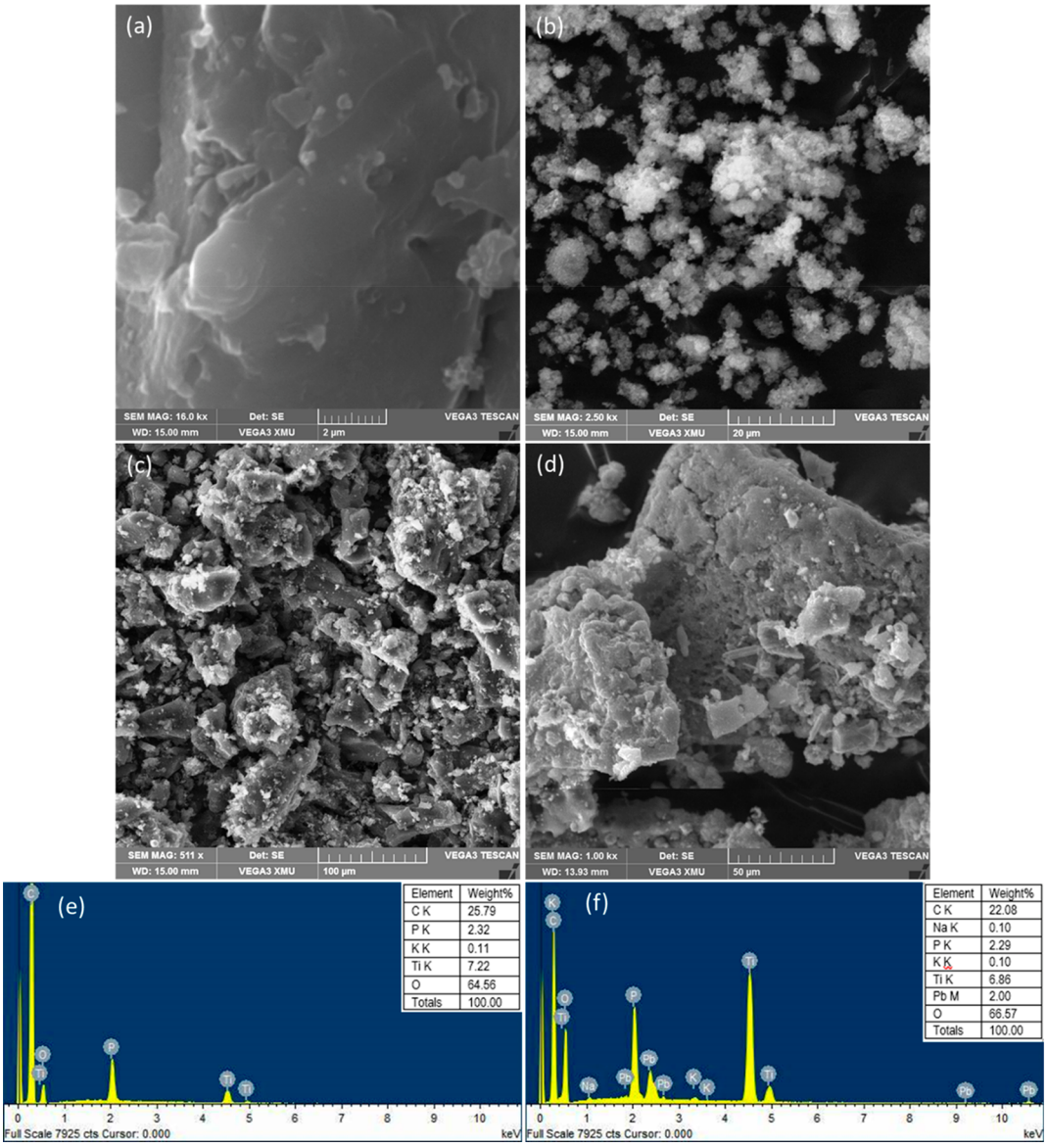

Figure 2. SEM images of (a) MC, (b) TiO_2 NPs, (c) the MC/TiO_2 NP nanocomposite, and (d) the Pb^{2+}-MC/TiO_2 NP nanocomposite. EDX spectrum of (e) the MC/TiO_2 NP nanocomposite and (f) the Pb^{2+}-MC/TiO_2 NP nanocomposite.

the mesoporous carbon samples, such as C═O, C−OH, and C−O. Figure 1c,i exhibits the peaks at 693.47 and 466.84 cm^{-1} corresponding to Ti−O vibrations and the Ti−O−C bond, respectively.[59,60] The presence of this Ti−O−C bond and the above-detected peaks indicate that the synthesis of a mesoporous carbon-coated TiO_2 NP nanocomposite was successful.

3.2. BET. BET was utilized to examine the surface area and total pore volume of MC and the MC/TiO_2 NP nanocomposite, as shown in Figure 1d, i and ii. The hysteresis loop shows the type IV model and the mesoporous nature of MC and the MC/TiO_2 NP nanocomposite.[61] The MC/TiO_2 NP nanocomposite has a specific BET surface area of 1283.822 m^2/g and a total pore volume of 3.94413 cm^3/g, Figure 1d, i, whereas MC has a BET surface area of 722.786 m^2/g and a large total pore volume of 0.578 cm^3/g, Figure 1d, ii. The surface area of the nanocomposite is higher than that of the mesoporous carbon. This suggests that TiO_2 NPs significantly increased the surface area and the binding site of MC for the removal of Pb^{2+} in wastewater.

3.3. TGA. A TGA plot was used to determine the thermal stability of MC and the MC/TiO_2 NP nanocomposite as depicted in Figure 1e. The initial weight loss, which ranged between 0.4 and 0.65%, is related to the material's loss of water. Under a nitrogen environment, the weight loss of MC and TiO_2 NP nanocomposites was measured up to 900 °C with a heating rate of 20 °C/min. The TGA shows a substantial weight reduction from 400 to 500 °C of the MC/TiO_2 NP nanocomposite and MC. The temperature with a maximum rate of weight loss is discovered to be 600 °C, which is the combustion point of the MC/TiO_2 NP nanocomposite. On the other hand, the MC burns until roughly 700 °C. This change may be attributed to the metal oxides grafted on the surface of MC, which may provide the reaction with the oxygen it needs and limit heat transfer, generating partial hot spots that facilitate the combustion of carbon.[62]

https://doi.org/10.1021/acsomega.2c05765
ACS Omega 2023, 8, 26725−26738

3.4. XRD. Figure 1a shows the XRD spectra of the MC samples. The two broad diffraction peaks in MC located at 2θ = 22.13° and 44.25° that were indexed at the (002) and (100) planes, respectively, clearly reveal the presence of amorphous carbon with disordered carbonaceous interlayers in Figure 2a.[63] Furthermore, these broad diffraction peaks were aligned with JCPDS No. 01-075-0444.[64] The diffractogram pattern confirmed an amorphous carbon that consists of random microcrystalline carbon fragments. The interlayer spacing d is calculated using the Bragg equation as shown in eq 4:

$$d = n\lambda/2 \sin\theta \quad (4)$$

where n = 1, λ is the X-ray wavelength (0.15406 nm), k = 1.54 Å is the incident X-ray wavelength, and θ is the peak position scattering angle. The crystallite size of both MC and the MC/TiO_2 NP nanocomposite are calculated from the Debye–Scherrer formula using eq 5:

$$D = K\lambda/\beta \cos\theta \quad (5)$$

where D is the crystalline size, B is the half-width of the peak in radians, λ = 0.15418 nm is the wavelength of the X-ray radiation, and K = 0.89 is the shape factor or equation constant. Figure 1b illustrates the diffraction peaks of the MC/TiO_2 NP nanocomposite, which exhibit peak positions of 2θ values at 17.15°, 25.52°, 37.98°, 47.92°, 54.60°, 62.75°, 75.43°, and 75.43°. These diffraction peaks can be indexed at (002), (101), (104), (200), (105), (211), (204), and (220), respectively. The peaks noted at 002 and 101 correspond to the MC and those at (104), (200), (105), (211), (204), and (220) to TiO_2 NPs.[65] These results further confirm the formation of a MC/TiO_2 NP nanocomposite. Based on the results, the MC/TiO_2 NP nanocomposite data correspond to JCPDS (JCPD No. 01-0562).[66] The particle size of the MC/TiO_2 NP nanocomposite is 4 nm, close to the results reported from TEM in Figure 4b, i and ii.

3.5. SEM. The surface morphological structures of MC, TiO_2 NPs, the MC/TiO_2 NP nanocomposite, and the Pb^{2+}-MC/TiO_2 NP nanocomposite were investigated using SEM and are shown in Figure 2a,b,c, and d, respectively. As reported by other researchers, a high surface area of MC was observed,[67] and the TiO_2 NPs and MC/TiO_2 NP nanocomposite are composed of nanoflowers[68,69] and spherical structures, respectively. The white particle in Figure 2b indicates the presence of TiO_2 NPs, and Figure 2c has a white granular particle and a black particle as an indication of both TiO_2 NPs and MC demonstrating successful binding of MC to TiO_2 NPs. Pb^{2+} ions are homogeneously embedded within the MC/TiO_2 NPS nanocomposite pores, as seen in Figure 2d. The EDX spectrum was used to examine the elemental composition of the MC/TiO_2 NP nanocomposite and Pb^{2+}-MC/TiO_2 NP nanocomposite, as shown in Figure 2e and f, respectively. The EDX spectrum of the MC/TiO_2 NP nanocomposite and Pb^{2+}-MC/TiO_2 NP nanocomposite indicates the presence of both C and Ti, and the presence of Ti and Pb was observed in Figure 2e and Figure 2f, respectively. It was evident that the entirety of the elements were well distributed on the surface of the MC/TiO_2 NP nanocomposite and Pb^{2+}-MC/TiO_2 NP nanocomposite.

3.6. TEM. Figure 3a, i and ii, and b, i and ii, display the TEM images of the synthesized MC and MC/TiO_2 NP nanocomposite, respectively. Figure 3a, i and ii, with a magnification of 100 and 50 nm confirms the structure of mesoporous carbon with a high surface area for Pb^{2+} to bind to the surface.[70−72] The spherical structures are noted in Figure 3b, i and ii, with a magnification of 50 and 100 nm; the black color denotes mesoporous carbon coated on white particles of TiO_2 NPs and therefore more binding sites on the surface of the adsorbent. The MC/TiO_2 NP nanocomposite consists of a 5 nm length and 5 nm width, and this confirms the nanomaterial range and the binding of MC to TiO_2 NPs, and the results agree with XRD.

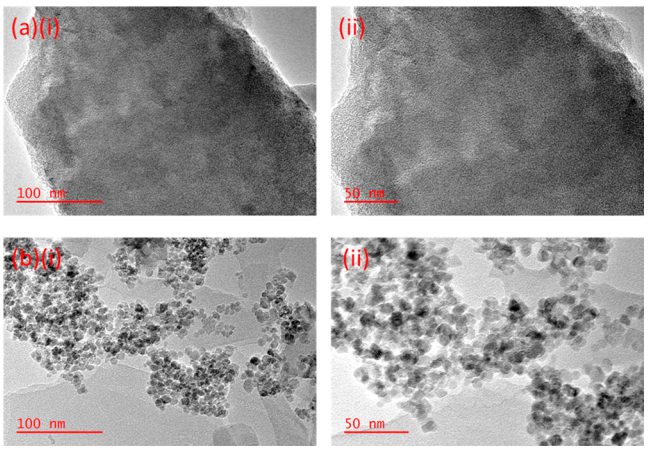

Figure 3. TEM images at different magnifications: (a, i) 100 nm to (ii) 50 nm MC, (b, i) 100 nm to (ii) 50 nm MC/TiO_2 NP nanocomposite.

3.7. Batch Adsorption Studies. *3.7.1. Effect of pH.* The pH is an important parameter that influences the adsorption of metal ions. The pH range was studied from 2 to 12 with an adsorbent dose of 2 g/L for 2 h at 25 °C, as shown in Figure 4a. The percentage removal reached the equilibrium at pH 4 with an increasing pH from 2 to 9, then dropped from 10 to 12. It shows that more charges are available in the solution of

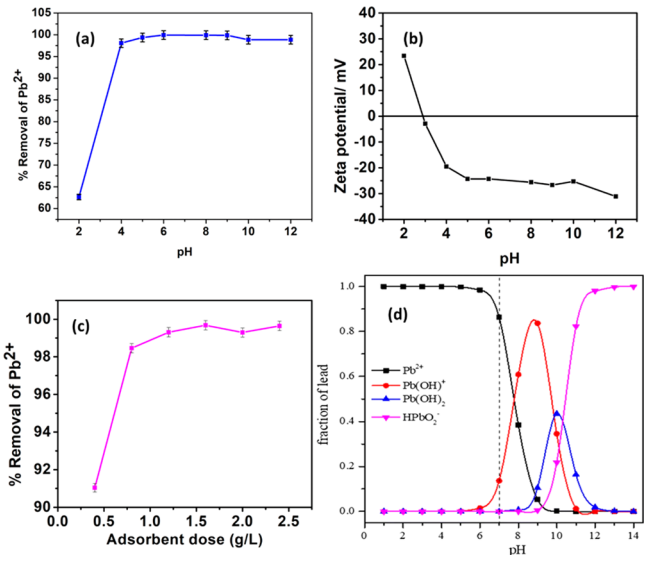

Figure 4. Plot of (a) the effect of pH (2−12, dosage of 2 g/L, Pb^{2+} ions of 20 ppm, T = 25 °C), (b) pH_{PZC}, (c) effect of adsorbent dose (0.4−2.4 g/L, Pb^{2+} ion of 20 ppm, pH 4, T = 25 °C). (d) Distribution of species as a function of pH and equilibriums of Pb^{2+} ions in aqueous medium.[76] The error bars represent the triplicate data's standard deviation. Adapted or reprinted in part with permission from ref 76. Copyright 2019, Springer Publishers.

https://doi.org/10.1021/acsomega.2c05765
ACS Omega 2023, 8, 26725−26738

Pb^{2+} to bind to the surface of the MC/TiO_2 NP nanocomposite. The removal rate gradually increased from pH 2 to 4 before reaching equilibrium. The findings confirmed that at a pH ≥ 7, the metal ions in water start to precipitate, which may affect the adsorption potential. However, at a pH below 7, adsorption is possible.[73] The highest removal rate was achieved at pH 4, with a removal percentage of 98%. From the plot of pH versus zeta potential, as shown in Figure 4b, the point of zero charge of the nanocomposite (PZC) was found to be 3.2. The point of zero charge determines the charge of the adsorbent surface. At a pH below 3.2, this shows that the surface of the adsorbent is negatively charged; there is an increase in adsorption with increasing pH, which is related to higher hydroxyl concentrations. However, as hydroxyl ions increase, precipitation sets in. In a noncomplex form, species (Pb^{2+}, $Pb(OH)^+$, $Pb(OH)_2$, and $Pb(OH)_3^-$) of lead ions in an aqueous solution occur in a wide pH range of 1−7.[74] As shown in the distribution of species in Figure 4d, hydroxy complexes occur at higher pH above 7, and this leads to the formation of insoluble lead hydroxide ($Pb(OH)_2$).[75,76]

3.7.2. Effect of Dosage. The effect of the dosage experiment was conducted by varying the MC/TiO_2 NP nanocomposite mass from 0.4 to 2.4 g/L at pH 4 for 2 h at 25 °C. The experiment was conducted to obtain the adsorption efficiency and determine the minimum mass required to remove Pb^{2+} in the solution. Figure 4c shows that the removal efficiency of Pb^{2+} by the MC/TiO_2 NP nanocomposite increased from 91 to 100% with an increasing adsorbent dose from 0.4 to 1.6 g/L. Still, it eventually levels off due to the saturation of binding sites. From 0.4 to 1.6 g/L, more active sites were bound to the surface of the MC/TiO_2 NP nanocomposite. It was shown that 1.6 g/L of MC/TiO_2 NP nanocomposite was the minimum dosage required for 98% removal of 20 ppm Pb^{2+} ions. From 1.6 g/L, equilibrium was reached, signifying no further adsorption.

3.7.3. Adsorption Isotherms. The adsorption isotherm is valuable in determining an efficient adsorption system's interaction between the adsorbent and adsorbate. The effect of temperature was studied at 25, 35, 45, and 55 °C at pH 4 using the adsorbent dose of 1.6 g/L for 2 h. The isotherm model is based on the interaction of the adsorbent and adsorbate.

The data obtained were further utilized to study the linear and nonlinear Langmuir eqs 6 and 7:

$$\frac{C_e}{q_e} = \frac{C_e}{q_m} + \frac{1}{k_L q_m} \tag{6}$$

$$q_e = \frac{K_L q_m C_e}{1 + K_L C_e} \tag{7}$$

where C_e is the equilibrium concentration of the Pb^{2+} solution, q_m is the maximum adsorption capacity, and q_e (mg g^{-1}) represents the amount of Pb^{2+} ions adsorbed at equilibrium. k_L (L g^{-1}) is the Langmuir constant.

The linear and nonlinear Freundlich, eqs 8 and 9, and Temkin isotherms, eq 10, were evaluated:

$$\ln q_e = \ln K_f + \frac{1}{n} \ln C_e \tag{8}$$

$$\ln q_e = K_f C_e^{1/n} \tag{9}$$

$$q_e = B \ln K_T + B \ln C_e \tag{10}$$

where $1/n$ and K_f is the Freundlich constant associated with the intensity of adsorption and adsorption capacity, k_T (L g^{-1}) represents the equilibrium binding constant that shows maximum binding energy, and B is the heat of adsorption constant. The linearized plot of fit on Figure 5a−c for Langmuir, Freundlich, and Temkin, respectively, has been plotted. Adsorption isotherm values were calculated and are shown in Table 1. Temkin was used to describe the relationship between adsorption energy and adsorbed metal ions. The Temkin with low heat energy values shows a weak interaction between Pb^{2+} and the MC/TiO_2 nanocomposite. The correlation coefficient (R^2) describes the suitability of these entire models.

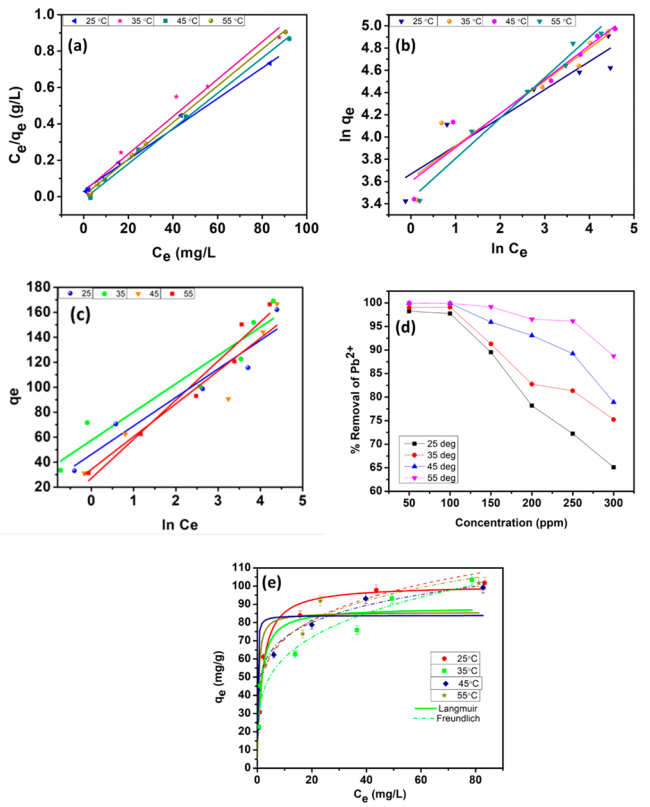

Figure 5. Fit of data to linear (a) Langmuir, (b) Freundlich, and (c) Temkin for Pb^{2+} adsorption by the MC/TiO_2 NP nanocomposite. (d) A plot of concentration versus temperature (50 to 300 ppm, pH 4, dosage of 1.6 g/L, T = 25 to 55 °C), data fit to nonlinear (e) Langmuir and Freundlich.

To determine the favorability of the adsorption process, eq 11 was used.

$$R_L = \frac{1}{1 + K_L C_o} \tag{11}$$

R_L is the separation factor, C_o is the initial metal ion concentration, and K_L is Langmuir's constant. If $0 < R_L < 1$, adsorption is favorable, and on the other hand, $R_L > 1$ articulates that the adsorption is unfavorable. $R_L = 0$ indicates irreversible adsorption, whereas $R_L = 1$ is linear adsorption. The data obtained in this study showed that the R_L of linear Langmuir was between 0 and 1, indicating that the adsorption is favorable for all temperatures.[77] In linear Freundlich, $n > 1$

https://doi.org/10.1021/acsomega.2c05765
ACS Omega 2023, 8, 26725−26738

Table 1. Isotherm Parameters for Adsorption of Pb^{2+} by MC/TiO_2 NP Nanocomposite (pH 4, Dosage of 1.6 g/L, Concentration of 50 to 300 ppm, T = 25 to 55 °C)

isotherm parameters	temperature 25 °C	35 °C	45 °C	55 °C
Langmuir				
linear				
q_m (mg/g)	119.617	142.248	89.127	168.919
k_L (L/mg)	0.231	0.195	1.001	1.052
R_L	0.080	0.093	0.020	0.019
R^2	0.944	0.965	0.975	0.993
nonlinear				
q_m (mg/g)	100.537	120.378	122.077	140.243
k_L (L/mg)	0.570	0.834	12.489	6.109
R^2	0.967	0.779	0.780	0.749
standard errors				
q_m (mg/g)	3.678	10.963	10.440	14.747
k_L (L/mg)	0.106	0.456	7.529	4.744
statistical data				
reduced χ-square	28.449	373.749	422.099	675.191
residual sum of squares	85.347	1494.994	1688.396	2700.762
degree of freedom	3	4	4	4
number of points	6	6	6	6
Freundlich				
linear				
k_f	39.126	47.036	72.287	87.259
$1/n$	0.253	0.248	0.154	0.202
R^2	0.858	0.874	0.666	0.974
nonlinear				
k_f	44.908	47.991	74.355	89.466
$1/n$	0.198	0.243	0.159	0.185
R^2	0.873	0.930	0.965	0.966
standard errors				
q_m (mg/g)	7.010	6.838	4.617	4.772
k_L (L/mg)	0.044	0.039	0.018	0.019
statistical data				
reduced χ-square	110.194	118.398	67.836	86.460
residual sum of squares	330.582	473.591	271.345	345.842
degree of freedom	3	4	4	4
number of points	5	6	6	6
Temkin				
k_T (L g^{-1})	8.873	15.470	1402.184	458.047
B_T (L g^{-1})	17.481	18.417	11.717	16.496
R^2	0.8532	0.900	0.510	0.952

suggests that the isotherm plot is favorable and a physical process. The $1/n > 1$ shows that the adsorption process is contrary. $1/n = 0$ to 1 signifies the homogeneity, and $1/n = 0$ shows that the adsorption is irreversible.[39] For this study, n is greater than 1, showing that it is a physical process and the isotherm model is favorable. The removal of Pb^{2+} ions occurs on the homogeneous media. The linear Langmuir q_m values ranged from 89.127 to 168.919 mg/g. For Langmuir, Freundlich, and Temkin with an R^2 value of 0.993, 0.974, and 0.952, respectively, the experimental data are better fitted by Langmuir with the highest R^2 signifying that the binding sites on the surface of MC/TiO_2 NP nanocomposite are homogeneous and monolayer, and a similar trend was observed in other studies.[78−82]

Table 2 is the comparative study of the adsorption capacity for different adsorbents utilized for Pb^{2+} removal. When comparing the MC/TiO_2 NP nanocomposite with other

Table 2. Comparison of the Adsorption Capacity of Pb^{2+} by MC/TiO_2 NPs Nanocomposite with Other Adsorbents

adsorbent	adsorption capacity (mg/g)	isotherms	references
ZnO/carbon nanofibers	92.590	Langmuir	86
chitosan/graphene oxide composites	76.940	Langmuir	87
activated carbon/nanoscale zerovalent iron composite	59.350	Langmuir	88
ZnO/montmorillonite	88.500	Langmuir	89
CDs/Al_2O_3 nanocomposite	177.830	Freundlich	90
ZnO@chitosan core/organically shell nanocomposite	476.100	Langmuir	91
MC/TiO_2 NP nanocomposite	168.919	Langmuir	this study

unmodified adsorbents, the adsorption capacity is very low compared to the chemically modified adsorbents due to few binding sites and a low surface area, whereas the modified one has greater binding and high surface area.[83−85] From Figure 5d, it was observed that the adsorption of Pb^{2+} was constant from 50 to 100 ppm and then decreased with increasing temperature (100 to 300 ppm), showing that the adsorption was exothermic. The optimum temperature effective for removal of Pb^{2+} was 55 °C with 99.98 to 99.90% at 50 to 100 ppm, respectively. The removal efficiency decreased when the concentration of Pb^{2+} increased from 100 ppm.

Figure 5e shows the linear and nonlinear adsorption isotherm plot of Langmuir and Freundlich. When comparing linear and nonlinear adsorption isotherms, the R^2_{linear} value (0.993) for Langmuir is higher compared to the Freundlich R^2_{linear} (0.974). Similarly, the q_m value for the linear (168.919 mg/g) is higher than the one of the reported linear Freundlich q_m (87.259), confirming linear Langmuir as the best fit.

3.7.4. Adsorption Kinetics. Adsorption kinetics are valuable in determining the adsorption rates to be considered for practical application or designing adsorption-based wastewater processes. The linear pseudo-first and second-order kinetic models were used and are represented by eqs 12 and 13.

$$\log(q_e - q_t) = \log(q_e) - \frac{K_1}{2.303}t \quad (12)$$

$$\frac{t}{q_t} = \frac{1}{K_2 q_e^2} + \frac{1}{q_e}t \quad (13)$$

where q_e (mg/g) and q_t (mg/g) represent the adsorption capacity at equilibrium and time t (min), respectively. Then, K_1 (1/min) and K_2 (g/mg/min) denote pseudo-first-order and pseudo-second-order order, respectively.

The kinetic data fitting linear pseudo-first-order and pseudo-second-order by adsorption of Pb^{2+} by the MC/TiO_2 NP nanocomposite with initial concentrations of 50, 100, 150, 200, 250, and 300 ppm were studied and are shown in Figure 6A and B, respectively. The kinetic parameter values for pseudo-first- and pseudo-second-order models were calculated and are presented in Table 3. From the data obtained, the pseudo-first-order kinetic plot in its linear form was inadequate to describe the kinetic behavior of adsorption of Pb^{2+} by the MC/TiO_2 NP nanocomposite with the lines not passing through the dots, and a similar trend was observed by other researchers.[92,93] The pseudo-second-order K_2 values decrease from 0.045 to 0.001 with increasing concentration, showing that the adsorption was slower at lower concentrations. A similar K_1 significant value

https://doi.org/10.1021/acsomega.2c05765
ACS Omega 2023, 8, 26725−26738

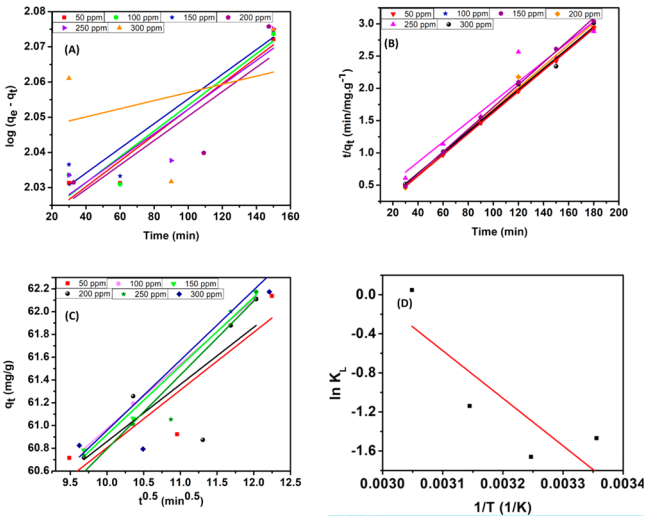

Figure 6. Plot of linearized data of (A) pseudo-first-order, (B) pseudo-second-order, and (C) intraparticle diffusion model (30 to 180 min, pH 4, dosage of 1.6 g/L, T = 55 °C). (D) Plot to obtain thermodynamic parameters for adsorption of Pb^{2+} by MC/TiO_2 NP nanocomposite.

for the Langmuir adsorption isotherm was observed elsewhere.[42,94] The R^2 value for the pseudo-second-order model (0.919−0.999) is higher than the R^2 value of the pseudo-first-order (0.480−0.883). Furthermore, the pseudo-second-order q_e calculated values are close to experimental values. However, this shows that the adsorption of Pb^{2+} by the MC/TiO_2 NP nanocomposite adsorbent fits the pseudo-second-order model better than the pseudo-first-order kinetic model.

To understand the rate-limiting step of the adsorption of Pb^{2+} by MC/TiO_2 NP nanocomposite, Weber and Morris' intraparticle diffusion model, eq 14, was employed.

$$q_t = K_i t^{0.5} + C \tag{14}$$

K_i is the intraparticle diffusion rate constant (mg/g/min$^{0.5}$), and C is the intercept of the boundary layer thickness (mg/g). The intraparticle diffusion model plots of $t^{0.5}$ versus q_t obtained from six different Pb^{2+} concentrations are shown in Figure 6C. The calculated values of K_i and C are shown in Table 3. The value of C is larger; this indicates that the boundary layer effect is greater. From the results obtained; the plots did not pass through the origin, as this suggests that the adsorption of Pb^{2+} by MC/TiO_2 NP nanocomposite shows that intraparticle diffusion does not contribute to the rate-limiting step and the relationship between the plot of q_t and $t^{0.5}$ was not reasonable. K_i values are not zero, as a result, it is also an indication that adsorption is not only controlled by intraparticle diffusion.[95]

3.7.5. Thermodynamic Study. Thermodynamic parameters, ΔG°, ΔS°, and ΔH°, related to the adsorption isotherm were calculated using eqs 15 and 16:

$$\Delta G^\circ = -RT \ln K_C = -RT \ln\left(m\frac{q_e}{C_e}\right) \tag{15}$$

$$\ln\left(m\frac{q_e}{C_e}\right) = \frac{\Delta S^\circ}{R} - \frac{\Delta H^\circ}{RT} \tag{16}$$

where R (J/mol K) is the gas constant, T is the temperature (K), m is the adsorbent dose (g/L), K_C is the equilibrium constant, and the ratio $m(q_e/C_e)$ is the affinity of the adsorption. The values of ΔG° were calculated from eq 15 and are shown in Table 4. ΔS° and ΔH° values were calculated from the slope (Table 4) and intercept of the plot of $\ln(m(q_e/C_e))$ versus $1/T$ as shown in Figure 7D. The negative value of ΔH° represents the exothermic nature of the Pb^{2+} removal by the MC/TiO_2 NP nanocomposite. The ΔS° negative value shows the binding of the adsorbent toward the adsorbate. The negative values of ΔG° with increasing temperature indicate that the adsorption process is spontaneous.

Table 4. Thermodynamic Parameters for Adsorption of Pb^{2+} by MC/TiO_2 NP Nanocomposite (30 to 180 min, pH 4, dosage of 1.6 g/L, T = 55 °C)

temperature (°C)	ΔG° (kJ/mol)	ΔH° (kJ/mol)	ΔS° (kJ/mol/K)
25	−4.743	−54.783	−166.785
35	−4.185		
45	−1.256		
55	−0.133		

Table 3. Adsorption Kinetics Data for Adsorption of Pb^{2+} by MC/TiO_2 NP Nanocomposite (30 to 180 min, pH 4, Dosage of 1.6 g/L, T = 55 °C)

	initial concentration (mg/L)					
kinetic parameters	50	100	150	200	250	300
pseudo-first-order						
R^2	0.883	0.827	0.809	0.480	0.647	0.802
K_1 (min^{-1})	8.44×10^{-4}	1.15×10^{-3}	1.61×10^{-3}	1.11×10^{-3}	7.25×10^{-3}	6.77×10^{-3}
q_e (exp; mg g^{-1})	31.014	62.119	87.475	110.101	135.509	142.264
q_e (calcd; mg g^{-1})	103.650	73.926	50.151	34.140	13.335	9.257
pseudo-second-order						
R^2	0.999	0.999	0.998	0.989	0.919	0.992
K_2 (g mg^{-1} min^{-1})	0.045	0.011	0.001	0.001	0.001	0.007
q_e (exp; mg g^{-1})	31.014	62.119	87.475	110.101	135.509	142.264
q_e (calcd; mg g^{-1})	30.553	61.767	86.881	111.982	137.741	142.248
intraparticle diffusion model						
R^2	0.660	0.998	0.984	0.516	0.895	0.591
C (mg/g)	29.552	59.877	82.509	87.898	92.864	128.068
k_i (mg/g/min$^{0.5}$)	0.112	0.168	0.367	1.483	3.102	1.804

https://doi.org/10.1021/acsomega.2c05765
ACS Omega 2023, 8, 26725−26738

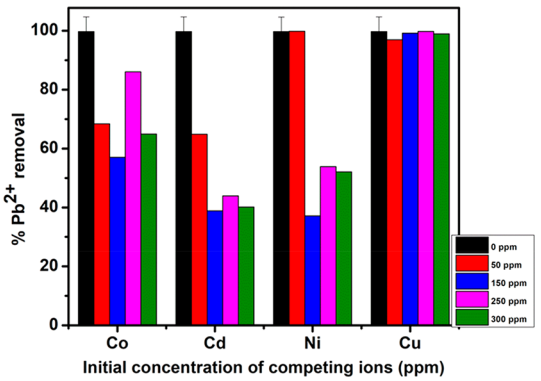

Figure 7. Effect of competing ions on Pb^{2+} ion adsorption.

3.8. Application of Real Wastewater. To test the efficient removal of metal ions in wastewater, the MC/TiO_2 NP nanocomposite was used to remove Pb^{2+} in real-world conditions. Wastewater was collected from the Daspoort wastewater treatment plant in Pretoria, Gauteng province, and stored in a refrigerator. The initial concentration was 0.246 ppm, and the pH of the wastewater was confirmed to be 7.38. The wastewater was spiked with 50 ppm of lead, and the pH was decreased to 4. An amount of 1.6 g/L of MC/TiO_2 NP nanocomposites was added and agitated in a shaker for 2 h at 180 rpm. The MC/TiO_2 NP nanocomposite can remove 98% of Pb^{2+} ions in water.

3.9. Effect of Coexisting Ions. Industrial effluent does not contain Pb^{2+} ions alone; it may contain other metal ions that lower the percentage removal of Pb^{2+} ions when competing for active adsorption sites. The effect of Co^{2+}, Cd^{2+}, Ni^{2+}, and Cu^{2+} on Pb^{2+} removal was studied, and the findings are shown in Figure 7. The concentration of Pb^{2+} was kept constant, and the other metal ions were varied from 0 to 300 ppm at pH 4. The metal ions are divalent, and an interaction with a charge on the surface of the MC/TiO_2 NP nanocomposite is possible. The results demonstrate that the presence of other ions influences the adsorption of Pb^{2+} onto the MC/TiO_2 NP nanocomposite. The presence of other metal ions can affect the adsorption capacity of Pb^{2+} ions in water, and Co^{2+} and Ni^{2+} influenced the efficiency of Pb^{2+}, with Cd^{2+} being the greatest. The order of influence of metal ions on Pb^{2+} with a charge per radius value (Z/R) was Cd^{2+} (2/0, 90) > Ni^{2+} (2/0, 70) > Co^{2+} > Cu^{2+} (2/0, 73).

3.10. Mechanism of Pb^{2+} Ions in the MC/TiO_2 NP Nanocomposite. The adsorption mechanism was studied to understand the Pb^{2+} and MC/TiO_2 NP nanocomposite interaction, Scheme 3. The high removal efficiency of Pb^{2+} was due to the increased surface area of the MC/TiO_2 NP nanocomposite. Ion exchange and pH_{pzc} were used to explore the adsorption mechanisms of Pb^{2+} further. In Figure 4a, the pH of the solution reached equilibrium at 4 using the MC/TiO_2 NP nanocomposite, which shows a possible mechanism

Scheme 3. Adsorption Mechanism of Pb^{2+} by Using the MC/TiO_2 NP Nanocomposite

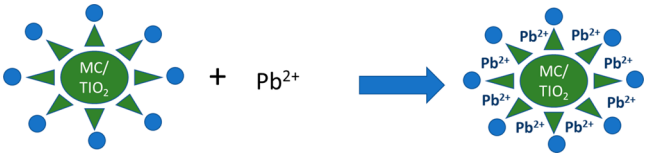

of Pb^{2+} on the surface of the MC/TiO_2 NP nanocomposite which involves a cation exchange of Pb^{2+} with H^+. From pH 4 to 12, no adsorption occurred due to the electrostatic interaction, indicating that all negative ions in the solution bonded to the positive ions on the surface of the MC/TiO_2 NP nanocomposite. Where pH > pH_{pzc}, this shows that more negative charges are on the MC/TiO_2 NP nanocomposite with protonation taking place.[42]

Electrostatic attraction:

$$MC\text{-}Ti(OH)_{3(s)} + OH^-_{(aq)} \rightarrow [MC\text{-}Ti(OH)_4]^-_{(S)}$$

$$[MC\text{-}Ti(OH)_4]^-_{(aq)} + Pb^{2+}_{(aq)} \rightarrow Pb^{2+}_{(s)} ...[MC\text{-}Ti(OH)_4]^-_{(S)}$$

Ion exchange rection:

$$[MC\text{-}TiOH]_{(s)} + Pb^{2+}_{(aq)} \rightarrow [MC\text{-}TiO\text{-}Pb]^+_{(aq)} + H^+_{(aq)}$$

3.11. Blood Detection by Pb^{2+}-MC/TiO_2 NP Nanocomposite. The Pb^{2+}-MC/TiO_2 NP nanocomposite was collected and reused to analyze blood fingerprint details (Scheme 4). The analysis was conducted under daylight on

Scheme 4. Blood Fingerprint Image Details by Pb^{2+}-MC/TiO_2 NP Nanocomposite on the Aluminum Sheet under Daylight Conditions

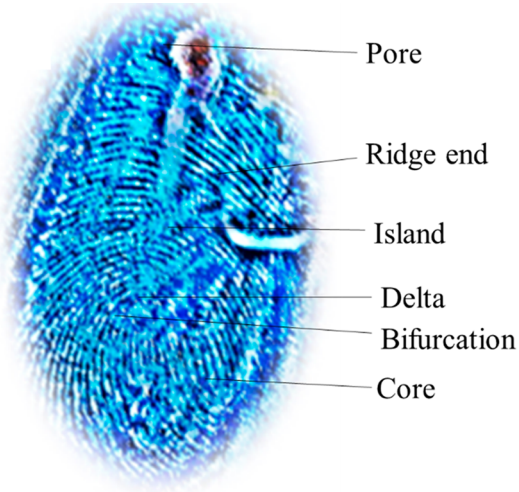

different nonporous surfaces, namely, glass, mirror, and aluminum sheets, before and after Pb^{2+}-MC/TiO_2 NP nanocomposite application, as depicted in Figure 8a,i. It was shown that the application of the Pb^{2+}-MC/TiO_2 NP nanocomposite improved the images on the mirror because of the clear fingerprint friction ridges observed. The images' nanocomposite surface on the glass slide and aluminum sheet were less clear. At a crime scene, blood fingerprints can be obtained on different substrates. As a result, we used glass to illustrate the suitability of the approach on windows, aluminum sheets for door handles and roof sheets, and mirrors for aluminum windows and doors, as well as an actual mirror. Materials on the nanoscale were selected as they became easy to bind to fingertips. Human fingertips have components such as amino acids, peptides, and fatty acids, and the focus of this study is the blood fingerprint. The visibility of ridges on the fingerprint shows that the Pb^{2+}-MC/TiO_2 NP nanocomposite attached to the blood on the fingertip. However, the appearance of the blood was not of paramount importance

https://doi.org/10.1021/acsomega.2c05765
ACS Omega 2023, 8, 26725−26738

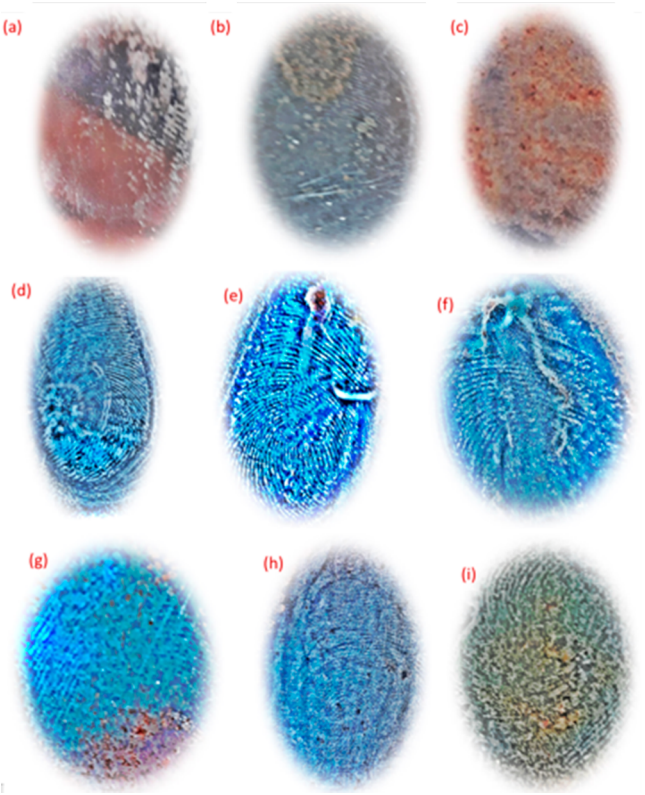

Figure 8. Photographs of blood fingerprints before application of the Pb^{2+}-MC/TiO_2 NP nanocomposite on (a) mirror, (b) aluminum sheet, (c) glass slides. Enhanced blood fingerprint using the Pb^{2+}-MC/TiO_2 NP nanocomposite on (d−f) mirror, (g,h) aluminum sheet, (i) glass slide.

since the study focused on enhancing the ridges/details on the fingertip. The reuse of the Pb^{2+}-MC/TiO_2 NP nanocomposite results in better friction ridges of fingermarks.

CONCLUSIONS

This study explored the removal of Pb^{2+} from wastewater using the MC/TiO_2 NP nanocomposite and tested the effectiveness of the Pb^{2+}-MC/TiO_2 NP nanocomposite in blood fingerprint detection. It was noted that the MC/TiO_2 NP nanocomposite was efficient and fast for the removal of Pb^{2+} in water, and the Pb^{2+}-MC/TiO_2 NP nanocomposite was further successful for reuse in latent blood fingerprint detection. The results proved the high surface area of MC and high adsorption capacity when coated with TiO_2 NPs. The MC/TiO_2 NP nanocomposite was confirmed to be in the nano range with a 5 nm length and 5 nm width. BET exhibited the surface area of 1283.822 m^2/g with good prospects that the MC/TiO_2 NP nanocomposite can treat wastewater. For the adsorption of Pb^{2+}, the maximum percentage removed by the MC/TiO_2 NP nanocomposite was achieved at pH 4 at 98%. The Langmuir isotherm model best described the adsorption behavior with a maximum adsorption capacity of 168.919 mg/g. The adsorption was suitable for a pseudokinetic model with a ΔH° value showing the exothermic nature and ΔG° indicating the spontaneous process. The ΔS° negative value shows the binding of the adsorbent toward the adsorbate. The Pb^{2+}-MC/TiO_2 NP nanocomposite was reused for blood fingerprint detection on different surfaces using the powder dusting method. The Pb^{2+}-MC/TiO_2 NP nanocomposite was proven to be an efficient labeling agent for detecting blood fingerprints that may be invisible at a crime scene. As a result, after removing Pb^{2+} from wastewater, it can be sold to law enforcement officials for use in latent blood fingerprint enhancement.

AUTHOR INFORMATION

Corresponding Author

Kriveshini Pillay − *Department of Chemical Sciences, University of Johannesburg, Johannesburg 2028, South Africa*; orcid.org/0000-0002-2134-7666; Email: kriveshinip@uj.ac.za

Authors

Yvonne Boitumelo Nthwane − *Department of Chemical Sciences, University of Johannesburg, Johannesburg 2028, South Africa*

Bienvenu Gael Fouda-Mbanga − *Department of Chemistry, Center for Rubber Science and Technology, Nelson Mandela University, Gqeberha 6031, South Africa*

Melusi Thwala − *Science Advisory and Strategic Partnerships, Academy of Science of South Africa, Pretoria 0040, South Africa; Department of Environmental Health, Nelson Mandela University, Port Elizabeth 6031, South Africa*

Complete contact information is available at: https://pubs.acs.org/10.1021/acsomega.2c05765

Notes

The authors declare no competing financial interest.

ACKNOWLEDGMENTS

The authors acknowledge the Department of Chemical Sciences, University of Johannesburg, South Africa. We would also like to thank the Department of Science and Technology/Council for scientific and industrial research, South Africa, for funding the research project.

REFERENCES

(1) Pratush, A.; Kumar, A.; Hu, Z. Adverse Effect of Heavy Metals (As, Pb, Hg, and Cr) on Health and Their Bioremediation Strategies: A Review. *Int. Microbiol.* **2018**, *21*, 97−106.

(2) Rehman, K.; Fatima, F.; Waheed, I.; Akash, M. S. H. Prevalence of Exposure of Heavy Metals and Their Impact on Health Consequences. *J. Cell. Biochem.* **2018**, *119*, 157−184.

(3) Gunatilake, S. K. Methods of Removing Heavy Metals from Industrial Wastewater. *Methods* **2015**, *1*, 14.

(4) Kumar, A.; Kumar, A.; M.M.S., C.-P.; Chaturvedi, A. K.; Shabnam, A. A.; Subrahmanyam, G.; Mondal, R.; Gupta, D. K.; Malyan, S. K.; Kumar, S. S.; A. Khan, S.; Yadav, K. K. others. Lead Toxicity: Health Hazards, Influence on Food Chain, and Sustainable Remediation Approaches. *Int. J. Environ. Res. Public Health.* **2020**, *17*, 2179.

(5) Jaishankar, M.; Tseten, T.; Anbalagan, N.; Mathew, B. B.; Beeregowda, K. N. Toxicity, Mechanism and Health Effects of Some Heavy Metals. *Interdiscip. Toxicol.* **2014**, *7*, 60.

(6) Pournara, A. D.; Rapti, S.; Lazarides, T.; Manos, M. J. A Dithiocarbamate-Functionalized Zr4+ MOF with Exceptional Capability for Sorption of Pb2+ in Aqueous Media. *J. Environ. Chem. Eng.* **2021**, *9*, 105474.

(7) Ucun, H.; Bayhana, Y. K.; Kaya, Y.; Cakici, A.; Algur, O. F. Biosorption of Lead (II) from Aqueous Solution by Cone Biomass of Pinus Sylvestris. *Desalination.* **2003**, *154*, 233−238.

(8) Goel, J.; Kadirvelu, K.; Rajagopal, C.; Kumar Garg, V. Removal of Lead (II) by Adsorption Using Treated Granular Activated Carbon: Batch and Column Studies. *J. Hazard. Mater.* **2005**, *125*, 211−220.

https://doi.org/10.1021/acsomega.2c05765
ACS Omega 2023, 8, 26725−26738

(9) South African Water Quality Guidelines. *Aquatic Ecosystems*, 1st ed.; Department of Water Affairs & Forestry, Pretoria; vol 7.
(10) Ozacar, M.; Sengil, I. A.; Turkmenler, H. Equilibrium and Kinetic Data, and Adsorption Mechanism for Adsorption of Lead onto Valonia Tannin Resin. *Chem. Eng. J.* **2008**, *143*, 32−42.
(11) Li, Y.; Xu, Z.; Liu, S.; Zhang, J.; Yang, X. Molecular Simulation of Reverse Osmosis for Heavy Metal Ions Using Functionalized Nanoporous Graphenes. *Comput. Mater. Sci.* **2017**, *139*, 65−74.
(12) Ates, N.; Uzal, N. Removal of Heavy Metals from Aluminum Anodic Oxidation Wastewaters by Membrane Filtration. *Environ. Sci. Pollut. Res.* **2018**, *25*, 22259−22272.
(13) Wu, R. Removal of Heavy Metal Ions from Industrial Wastewater Based on Chemical Precipitation Method. *Ekoloji* **2019**, *28*, 2443−2452.
(14) Barakat, M. A.; Ismat-Shah, S. Utilization of Anion Exchange Resin Spectra/Gel for Separation of Arsenic from Water. *Arabian J. Chem.* **2013**, *6*, 307−311.
(15) Sharma, S.; Rana, S.; Thakkar, A.; Baldi, A.; Murthy, R. S. R.; Sharma, R. K. Physical, Chemical and Phytoremediation Technique for Removal of Heavy Metals. *J. heavy met. toxic. dis.* **2016**, *1*, 1−15.
(16) Feng, Q.; Zhang, Z.; Chen, Y.; Liu, L.; Zhang, Z.; Chen, C. Adsorption and Desorption Characteristics of Arsenic on Soils: Kinetics, Equilibrium, and Effect of Fe (OH) 3 Colloid, H2SiO3 Colloid and Phosphate. *Procedia. Environ. Sci.* **2013**, *18*, 26−36.
(17) Guerrero, G. I.; Moreno, E. G. Design of Experiments for Evaluation of Variables Involved in the Removal of Heavy Metal Ions From Water Using Agro-Industrial Waste-Based Adsorbents. In *Design of Experiments for Chemical, Pharmaceutical, Food, and Industrial Applications*; IGI Global, 2020; pp 53−76.
(18) Al-Othman, Z. A.; Ali, R.; Naushad, M. Hexavalent Chromium Removal from Aqueous Medium by Activated Carbon Prepared from Peanut Shell: Adsorption Kinetics, Equilibrium and Thermodynamic Studies. *Chem. Eng. J.* **2012**, *184*, 238−247.
(19) Khan, S.; Idrees, M.; Bilal, M. Revealing and Elucidating Chemical Speciation Mechanisms for Lead and Nickel Adsorption on Zeolite in Aqueous Solutions. *Colloids. Surf. A Physicochem. Eng. Asp.* **2021**, *623*, 126711.
(20) Kongsune, P.; Rattanapan, S.; Chanajaree, R. The Removal of Pb2+ from Aqueous Solution Using Mangosteen Peel Activated Carbon: Isotherm, Kinetic, Thermodynamic and Binding Energy Calculation. *Groundw. Sustain. Dev.* **2021**, *12*, 100524.
(21) Basu, M.; Guha, A. K.; Ray, L. Adsorption of Lead on Cucumber Peel. *J. Clean. Prod.* **2017**, *151*, 603−615.
(22) Taşar, E.; Kaya, F.; Özer, A. Biosorption of Lead(II) Ions from Aqueous Solution by Peanut Shells: Equilibrium, Thermodynamic and Kinetic Studies. *J. Environ. Chem. Eng.* **2014**, *2*, 1018−1026.
(23) Chakravarty, S.; Mohanty, A.; Sudha, T. N.; Upadhyay, A. K.; Konar, J.; Sircar, J. K.; Madhukar, A.; Gupta, K. K. Removal of Pb(II) Ions from Aqueous Solution by Adsorption Using Bael Leaves (Aegle Marmelos). *J. Hazard. Mater.* **2010**, *173*, 502−509.
(24) Elias, M. A.; Hadibarata, T.; Sathishkumar, P. Modified Oil Palm Industry Solid Waste as a Potential Adsorbent for Lead Removal. *Environ. Chem. Ecotoxicol.* **2021**, *3*, 1−7.
(25) Dixit, A.; Mishra, P. K.; Alam, M. S. Titania Nanofibers: A Potential Adsorbent for Mercury and Lead Uptake. *Int. J. Chem. Eng. Appl.* **2017**, *8*, 75.
(26) Vilas Boas, N.; Casarin, J.; Passarella Gerola, G.; Ricardo Teixeira Tarley, C.; Caetano, J.; Celso Gonçalves, A., Jr; Cardoso Dragunski, D. Evaluation of Kinetic and Thermodynamic Parameters in Adsorption of Lead (Pb2+) and Chromium (Cr3+) by Chemically Modified Macadamia (Macadamia Integrifolia). *Desalination. Water. Treat.* **2016**, *57*, 17738−17747.
(27) Pakade, V. E.; Ntuli, T. D.; Ofomaja, A. E. Biosorption of Hexavalent Chromium from Aqueous Solutions by Macadamia Nutshell Powder. *Appl. Water. Sci.* **2017**, *7*, 3015−3030.
(28) Dao, M. T.; Nguyen, T. T.; Nguyen, X. du; La, D. D.; Nguyen, D. D.; Chang, S. W.; Chung, W. J.; Nguyen, V. K. others. Toxic Metal Adsorption from Aqueous Solution by Activated Biochars Produced from Macadamia Nutshell Waste. *Sustainability.* **2020**, *12*, 7909.
(29) Mogala, M. A Profile of the South African Macadamia Nuts Market Value Chain 2014. Department of Agriculture, Forestry and Fishers, Republic of South Africa, 2014.
(30) Maremeni, L. C.; Modise, S. J.; Mtunzi, F. M.; Klink, M. J.; Pakade, V. E. Adsorptive Removal of Hexavalent Chromium by Diphenylcarbazide-Grafted Macadamia Nutshell Powder. *Bioinorg. Chem. Appl.* **2018**, *2018*, 1.
(31) Azwar, E.; Wan Mahari, W. A.; Chuah, J. H.; Vo, D.-V. N.; Ma, N. L.; Lam, W. H.; Lam, S. S. Transformation of Biomass into Carbon Nanofiber for Supercapacitor Application-a Review. *Int. J. Hydrogen Energy.* **2018**, *43*, 20811−20821.
(32) Mousavi, S. V.; Bozorgian, A.; Mokhtari, N.; Gabris, M. A.; Rashidi Nodeh, H.; Wan Ibrahim, W. A. A Novel Cyanopropylsilane-Functionalized Titanium Oxide Magnetic Nanoparticle for the Adsorption of Nickel and Lead Ions from Industrial Wastewater: Equilibrium, Kinetic and Thermodynamic Studies. *Microchem. J.* **2019**, *145*, 914−920.
(33) Kwon, H.; Marques Mota, F.; Chung, K.; Jang, Y. J.; Hyun, J. K.; Lee, J.; Kim, D. H. Enhancing Solar Light-Driven Photocatalytic Activity of Mesoporous Carbon-TiO2 Hybrid Films via Upconversion Coupling. *ACS Sustainable Chem. Eng.* **2018**, *6*, 1310−1317.
(34) Liu, S.; Li, C.; Liu, D. Modified Separator Based on Mesoporous Carbon/TiO2 Composites as Advanced Polysulfide Adsorber for High Electrochemical Performance Li-S Batteries. *J. Alloys. Compd.* **2021**, *862*, 158381.
(35) Cai, H.; Liang, P.; Hu, Z.; Shi, L.; Yang, X.; Sun, J.; Xu, N.; Wu, J. Enhanced Photoelectrochemical Activity of ZnO-Coated TiO2 Nanotubes and Its Dependence on ZnO Coating Thickness. *Nanoscale. Res. Lett.* **2016**, *11*, 1−11.
(36) Gnanasekar, K.; Rambabu, B. Nanostructure Semiconductor Oxide Powders and Thin Films for Gas Sensor. *Surf. Sci.* **2002**, *200*, 780.
(37) Haider, A. J.; Jameel, Z. N.; Al-Hussaini, I. H. M. Review on: Titanium Dioxide Applications. *Energy Procedia.* **2019**, *157*, 17−29.
(38) Ballav, N.; Das, R.; Giri, S.; Muliwa, A. M.; Pillay, K.; Maity, A. L-Cysteine Doped Polypyrrole (PPy@L-Cyst): A Super Adsorbent for the Rapid Removal of Hg+2 and Efficient Catalytic Activity of the Spent Adsorbent for Reuse. *Chem. Eng. J.* **2018**, *345*, 621−630.
(39) He, D.; Zhang, Y.; Yang, S.; Zhang, L.; Lu, J.; Zhao, Y.; Mei, Y.; Han, C.; Luo, Y. Development of a Strategy to Reuse Spent Cr Adsorbents as Efficient Catalysts: From the Perspective of Practical Application. *ACS Sustainable Chem. Eng.* **2019**, *7*, 3251−3257.
(40) Umejuru, E. C.; Prabakaran, E.; Pillay, K. Coal Fly Ash Coated with Carbon Hybrid Nanocomposite for Remediation of Cadmium (II) and Photocatalytic Application of the Spent Adsorbent for Reuse. *Results Mater.* **2020**, *7*, 100117.
(41) Umejuru, E. C.; Prabakaran, E.; Pillay, K. Coal Fly Ash Decorated with Graphene Oxide-Tungsten Oxide Nanocomposite for Rapid Removal of Pb2+Ions and Reuse of Spent Adsorbent for Photocatalytic Degradation of Acetaminophen. *ACS Omega.* **2021**, *6*, 11155−11172.
(42) Fouda-Mbanga, B. G.; Prabakaran, E.; Pillay, K. Synthesis and Characterization of CDs/Al2O3 Nanofibers Nanocomposite for Pb2+ Ions Adsorption and Reuse for Latent Fingerprint Detection. *Arabian J. Chem.* **2020**, *13*, 6762−6781.
(43) Fouda-Mbanga, B.; Prabakaran, E.; Pillay, K. Cd2+ Ion Adsorption and Re-Use of Spent Adsorbent with N-Doped Carbon Nanoparticles Coated on Cerium Oxide Nanorods Nanocomposite for Fingerprint Detection. *Chemical Physics Impact.* **2022**, *5*, 100083.
(44) Mofulatsi, M. W.; Prabakaran, E.; Velempini, T.; Green, E.; Pillay, K. Preparation of Manganese Oxide Coated Coal Fly Ash Adsorbent for the Removal of Lead and Reuse for Latent Fingerprint Detection. *Microporous Mesoporous Mater.* **2022**, *329*, 111480.
(45) Qiu, Z.; Hao, B.; Gu, X.; Wang, Z.; Xie, N.; Lam, J. W. Y.; Hao, H.; Tang, B. Z. A General Powder Dusting Method for Latent Fingerprint Development Based on AIEgens. *Sci. China. Chem.* **2018**, *61*, 966−970.

https://doi.org/10.1021/acsomega.2c05765
ACS Omega 2023, 8, 26725−26738

(46) Fernandes, D.; Krysmann, M. J.; Kelarakis, A. Carbogenically Coated Silica Nanoparticles and Their Forensic Applications. *Chem. Commun.* **2016**, *52*, 8294−8296.
(47) Zhao, Y.-B.; Ma, Y.; Song, D.; Liu, Y.; Luo, Y.; Lin, S.; Liu, C. New Luminescent Nanoparticles Based on Carbon Dots/SiO2 for the Detection of Latent Fingermarks. *Anal. Methods.* **2017**, *9*, 4770−4775.
(48) Becue, A.; Moret, S.; Champod, C.; Margot, P. Use of Quantum Dots in Aqueous Solution to Detect Blood Fingermarks on Non-Porous Surfaces. *Forensic. Sci. Int.* **2009**, *191*, 36−41.
(49) SHUI, J.; LIU, W. Comparative Study of Amido Black, Titanium Dioxide (TiO_2) and Acid Yellow 7 for Development of Blood Fingerprint on Non-Porous Surface. *Forensic. Sci. and Technol.* **2014**, 2.
(50) Sodhi, G. S.; Kaur, J. Powder Method for Detecting Latent Fingerprints: A Review. *Forensic. Sci. Int.* **2001**, *120*, 172−176.
(51) Jin, X.; Xin, R.; Wang, S.; Yin, W.; Xu, T.; Jiang, Y.; Ji, X.; Chen, L.; Liu, J. A Tetraphenylethene-Based Dye for Latent Fingerprint Analysis. *Sens. Actuators. B. Chem.* **2017**, *244*, 777−784.
(52) Wang, M.; Li, M.; Yu, A.; Zhu, Y.; Yang, M.; Mao, C. Fluorescent Nanomaterials for the Development of Latent Fingerprints in Forensic Sciences. *Adv. Funct. Mater.* **2017**, *27*, 1606243.
(53) Becue, A.; Scoundrianos, A.; Champod, C.; Margot, P. Fingermark Detection Based on the in Situ Growth of Luminescent Nanoparticles—Towards a New Generation of Multimetal Deposition. *Forensic. Sci. Int.* **2008**, *179*, 39−43.
(54) Ran, X.; Wang, Z.; Zhang, Z.; Pu, F.; Ren, J.; Qu, X. Nucleic-Acid-Programmed Ag-Nanoclusters as a Generic Platform for Visualization of Latent Fingerprints and Exogenous Substances. *Chem. Commun.* **2016**, *52*, 557−560.
(55) Lee, J.; Lee, C. W.; Kim, J. M. A Magnetically Responsive Polydiacetylene Precursor for Latent Fingerprint Analysis. *ACS Appl. Mater. Interfaces.* **2016**, *8*, 6245−6251.
(56) Benzigar, M. R.; Talapaneni, S. N.; Joseph, S.; Ramadass, K.; Singh, G.; Scaranto, J.; Ravon, U.; Al-Bahily, K.; Vinu, A. Recent Advances in Functionalized Micro and Mesoporous Carbon Materials: Synthesis and Applications. *Chem. Soc. Rev.* **2018**, *47*, 2680−2721.
(57) Lv, X.; Liu, C.; Song, S.; Qiao, Y.; Hu, Y.; Li, P.; Li, Z.; Sun, S. *Construction of a Quaternary Ammonium Salt Platform with Different Alkyl Groups for Antibacterial and Biosensor Applications* **2018**, *8*, 2941.
(58) Hubetska, T.; Kobylinska, N.; García, J. R. Efficient Adsorption of Pharmaceutical Drugs from Aqueous Solution Using a Mesoporous Activated Carbon. *Adsorption.* **2020**, *26*, 251−266.
(59) Mombeshora, E. T.; Simoyi, R.; Nyamori, V. O.; Ndungu, P. G. Multiwalled Carbon Nanotube-Titania Nanocomposites: Understanding Nano-Structural Parameters and Functionality in Dye-Sensitized Solar Cells. *South African Journal of Chemistry* **2015**, *68*, 153−164.
(60) Ahmad, A.; Razali, M. H.; Mamat, M.; Mehamod, F. S. B.; Anuar Mat Amin, K. Adsorption of Methyl Orange by Synthesized and Functionalized-CNTs with 3-Aminopropyltriethoxysilane Loaded TiO2 Nanocomposites. *Chemosphere.* **2017**, *168*, 474−482.
(61) Xu, L.; Zhang, J.; Ding, J.; Liu, T.; Shi, G.; Li, X.; Dang, W.; Cheng, Y.; Guo, R. Pore Structure and Fractal Characteristics of Different Shale Lithofacies in the Dalong Formation in the Western Area of the Lower Yangtze Platform. *Minerals.* **2020**, *10*, 72.
(62) Yin, B.; Wang, J. T.; Xu, W.; Long, D. H.; Qiao, W. M.; Ling, L. C. Preparation of TiO2/Mesoporous Carbon Composites and Their Photocatalytic Performance for Methyl Orange Degradation. *New Carbon Mater.* **2013**, *28*, 47−54.
(63) Morifi, E.; Chimuka, L.; Richards, H.; Senyolo, L.; Pillay, K. Modified Macadamia Nutshell Nanocomposite for Selective Removal of Hexavalent Chromium from Wastewater. *S. Afr. J. Chem. Eng.* **2022**, *42*, 176−187.
(64) Duraisamy, V.; Palanivel, S.; Thangamuthu, R.; Kumar, S. M. S. KIT-6 Three Dimensional Template Derived Mesoporous Carbon for Oxygen Reduction Reaction: Effect of Template Removal on Catalytic Activity. *ChemistrySelect.* **2018**, *3*, 11864−11874.
(65) Toro, R. G.; Diab, M.; de Caro, T.; Al-Shemy, M.; Adel, A.; Caschera, D. Study of the Effect of Titanium Dioxide Hydrosol on the Photocatalytic and Mechanical Properties of Paper Sheets. *Materials. 2020, Vol. 13, Page 1326* **2020**, *13*, 1326.
(66) Ryu, M.-H.; Jung, K.-N.; Shin, K.-H.; Han, K.-S.; Yoon, S. High Performance N-Doped Mesoporous Carbon Decorated TiO 2 Nanofibers as Anode Materials for Lithium-Ion Batteries. *J. Phys. Chem. C* **2013**, *117*, 8092.
(67) Li, G.; Cai, W.; Zhao, R.; Hao, L. Electrosorptive Removal of Salt Ions from Water by Membrane Capacitive Deionization (MCDI): Characterization, Adsorption Equilibrium, and Kinetics. *Environ. Sci. Pollut. Res.* **2019**, *26*, 17787−17796.
(68) Roy, H. G. Optical Properties And Photo Catalytic Activities Of Titania Nanoflowers Synthesized By Microwave Irradiation. *Int. J. Innov. Res. Sci. Eng. Technol.* **2013**, *2*, 2175−2181.
(69) Baghban, N.; Haji Shabani, A. M.; Dadfarnia, S. Solid Phase Extraction and Flame Atomic Absorption Spectrometric Determination of Trace Amounts of Cadmium and Lead in Water and Biological Samples Using Modified TiO2 Nanoparticles. *Int. J. Environ. Anal. Chem.* **2013**, *93*, 1367−1380.
(70) Eftekhari, A.; Fan, Z. Ordered Mesoporous Carbon and Its Applications for Electrochemical Energy Storage and Conversion. *Mater. Chem. Front.* **2017**, *1*, 1001−1027.
(71) Samiee, L.; Tasharrofi, S.; Hassani, S. S.; Fardi, M.; Mazinani, B. Novel and Economic Approach for Synthesis of Mesoporous Silica Template and Ordered Carbon Mesoporous by Using Cation Exchange Resin. *Curr. Nanosci.* **2017**, *13*, 595−603.
(72) Qin, H.; Jian, R.; Bai, J.; Tang, J.; Zhou, Y.; Zhu, B.; Zhao, D.; Ni, Z.; Wang, L.; Liu, W.; Zhou, Q.; Li, X. others. Influence of Molecular Weight on Structure and Catalytic Characteristics of Ordered Mesoporous Carbon Derived from Lignin. *ACS Omega.* **2018**, *3*, 1350−1356.
(73) Çelebi, H.; Gök, G.; Gök, O. Adsorption Capability of Brewed Tea Waste in Waters Containing Toxic Lead (II), Cadmium (II), Nickel (II), and Zinc (II) Heavy Metal Ions. *Sci. Rep.* **2020**, *10*, 1−12.
(74) Fayazi, M.; Afzali, D.; Ghanei-Motlagh, R.; Iraji, A. Synthesis of Novel Sepiolite-Iron Oxide-Manganese Dioxide Nanocomposite and Application for Lead(II) Removal from Aqueous Solutions. *Environ. Sci. Pollut. Res.* **2019**, *26*, 18893−18903.
(75) Fayazi, M.; Afzali, D.; Ghanei-Motlagh, R.; Iraji, A. Synthesis of Novel Sepiolite-Iron Oxide-Manganese Dioxide Nanocomposite and Application for Lead(II) Removal from Aqueous Solutions. *Environ. Sci. Pollut. Res.* **2019**, *26*, 18893−18903.
(76) Oliveira, L. C.; Botero, W. G.; Farias, T. S.; Santos, J. C. C.; Gabriel, G. V. M.; Goveia, D.; Cacuro, T. A.; Waldman, W. R. Application of Natural Organic Residues as Adsorbents to Remove Lead from Waters. *Water. Air. Soil. Pollut.* **2019**, *230*, 1−11.
(77) Cheng, S.; Zhao, S.; Guo, H.; Xing, B.; Liu, Y.; Zhang, C.; Ma, M. High-Efficiency Removal of Lead/Cadmium from Wastewater by MgO Modified Biochar Derived from Crofton Weed. *Bioresour. Technol.* **2022**, *343*, 126081.
(78) Pathan, S.; Pandita, N.; Kishore, N. Acid Functionalized-Nanoporous Carbon/MnO2 Composite for Removal of Arsenic from Aqueous Medium. *Arabian J. Chem.* **2019**, *12*, 5200−5211.
(79) Ifijen, I. H.; Itua, A. B.; Maliki, M.; Ize-Iyamu, C. O.; Omorogbe, S. O.; Aigbodion, A. I.; Ikhuoria, E. U. The Removal of Nickel and Lead Ions from Aqueous Solutions Using Green Synthesized Silica Microparticles. *Heliyon.* **2020**, *6*, e04907.
(80) Khan, T.; Binti Abd Manan, T. S.; Isa, M. H.; Ghanim, A. A. J.; Beddu, S.; Jusoh, H.; Iqbal, M. S.; Ayele, G. T; Jami, M. S. Modeling of Cu(II) Adsorption from an Aqueous Solution Using an Artificial Neural Network (ANN). *Molecules* **2020**, *25*, 3263.
(81) Singh, H.; Jain, A.; Kaur, J.; Arya, S. K.; Khatri, M. Adsorptive Removal of Oil from Water Using SPIONs-Chitosan Nanocomposite: Kinetics and Process Optimization. *Appl. Nanosci. (Switzerland)* **2020**, *10*, 1281−1295.
(82) Murshed, M. F.; Mohammadpour, R.; Chow, C. Comparing the Log-Response Curve and Adsorption Isotherm Model for Removing

https://doi.org/10.1021/acsomega.2c05765
ACS Omega 2023, 8, 26725−26738

Dissolved Organic Matter during La Nina Event. *Water Environ. J.* **2021**, *35*, 133−147.
(83) Nwagbara, V. U.; Chigayo, K.; Iyama, W. A.; Kwaambwa, H. M. Removal of Lead, Cadmium, and Copper from Water Using Moringa Oleifera Seed Biomass. *J. Water Clim. Change.* **2022**, *13*, 2747−2760.
(84) Taib, N. I.; Rosli, N. A.; Saharrudin, N. I.; Rozi, N. M.; Kasdiehram, N. A. A.; Abu Nazri, N. N. T. Kinetic, Equilibrium, and Thermodynamic Studies of Untreated Watermelon Peels for Removal of Copper(II) from Aqueous Solution. *Desalin. Water Treat.* **2021**, *227*, 289−299.
(85) Afolabi, F. O.; Musonge, P.; Bakare, B. F. Application of the Response Surface Methodology in the Removal of Cu2+ and Pb2+ from Aqueous Solutions Using Orange Peels. *Sci. Afr.* **2021**, *13*, No. e00931.
(86) Ibupoto, A. S.; Qureshi, U. A.; Arain, M.; Ahmed, F.; Khatri, Z.; Brohi, R. Z.; Kim, I. S.; Ibupoto, Z. Zno/Carbon Nanofibers for Efficient Adsorption of Lead from Aqueous Solutions. *Environ. Technol.* **2020**, *41*, 2731.
(87) Fan, L.; Luo, C.; Sun, M.; Li, X.; Qiu, H. Highly Selective Adsorption of Lead Ions by Water-Dispersible Magnetic Chitosan/Graphene Oxide Composites. *Colloids. Surf. B. Biointerfaces.* **2013**, *103*, 523−529.
(88) Liu, X.; Lai, D.; Wang, Y. Performance of Pb (II) Removal by an Activated Carbon Supported Nanoscale Zero-Valent Iron Composite at Ultralow Iron Content. *J. Hazard. Mater.* **2019**, *361*, 37−48.
(89) Sani, H. A.; Ahmad, M. B.; Hussein, M. Z.; Ibrahim, N. A.; Musa, A.; Saleh, T. A. Nanocomposite of ZnO with Montmorillonite for Removal of Lead and Copper Ions from Aqueous Solutions. *Process Saf. Environ. Prot.* **2017**, *109*, 97−105.
(90) Fouda-Mbanga, B. G.; Prabakaran, E.; Pillay, K. Synthesis and Characterization of CDs/Al2O3 Nanofibers Nanocomposite for Pb2+ Ions Adsorption and Reuse for Latent Fingerprint Detection. *Arabian J. Chem.* **2020**, *13*, 6762−6781.
(91) Saad, A. H. A.; Azzam, A. M.; El-Wakeel, S. T.; Mostafa, B. B.; Abd El-latif, M. B. Removal of Toxic Metal Ions from Wastewater Using ZnO@ Chitosan Core-Shell Nanocomposite. *Environ. Nanotechnol., Monit. Manage.* **2018**, *9*, 67−75.
(92) Aden, M.; Husson, J.; Monney, S.; Franchi, M.; Knorr, M.; Euvrard, M. Biosorption of Pb(II) Ions from Aqueous Solution Using Alginates Extracted from Djiboutian Seaweeds and Deposited on Silica Particles. *Pure Appl. Chem.* **2019**, *91*, 459−475.
(93) Wang, G.; Zhang, S.; Yao, P.; Chen, Y.; Xu, X.; Li, T.; Gong, G. Removal of Pb(II) from Aqueous Solutions by Phytolacca Americana L. Biomass as a Low Cost Biosorbent. *Arabian J. Chem.* **2018**, *11*, 99−110.
(94) Umejuru, E. C.; Prabakaran, E.; Pillay, K. Coal Fly Ash Decorated with Graphene Oxide-Tungsten Oxide Nanocomposite for Rapid Removal of Pb2+Ions and Reuse of Spent Adsorbent for Photocatalytic Degradation of Acetaminophen. *ACS Omega.* **2021**, *6*, 11155−11172.
(95) Jain, M.; Yadav, M.; Kohout, T.; Lahtinen, M.; Garg, V. K.; Sillanpää, M. Development of Iron Oxide/Activated Carbon Nanoparticle Composite for the Removal of Cr(VI), Cu(II) and Cd(II) Ions from Aqueous Solution. *Water. Resour. Ind.* **2018**, *20*, 54−74.

https://doi.org/10.1021/acsomega.2c05765
ACS Omega 2023, 8, 26725−26738